Preprints of the 19th World Congress
The International Federation of Automatic Control
Cape Town, South Africa. August 24-29, 2014

Nonlinear State Estimation in the Czochralski Process ⋆

Parsa Rahmanpour * **Morten Hovd** ** **John Atle Bones** ***

* *Dept. of Engineering Cybernetics, Norwegian Univ. of Science and Technology (NTNU), NO-7491 Trondheim, Norway.* (e-mail: parsa.rahmanpour@itk.ntnu.no).
** *Dept. of Engineering Cybernetics, (NTNU)*
*** *SINTEF, Materials and Chemistry, Trondheim, Norway*

Abstract: The Czochralski process is the only process used commercially for production of monocrystalline silicon for semiconductor and solar cell applications. The process has traditionally been controlled using nested single-loop PID controllers. Advanced model-based control will require the ability to update the model used for control by using the measurements available on-line. This paper presents a study of non-linear state estimation based on a previously developed non-linear dynamical model. Data from actual plant operation are used in the study. Most application studies on state estimation only have on-line, noise corrupted/uncertain measurements available. In this case, the crystal radius as the main process variable, can be measured with much greater accuracy after the crystal is produced. It is therefore possible to assess estimator performance using this more accurate off-line measurement. The experimental results in this work confirm the simulation results from a preceding paper and show that the applied non-linear estimators perform well, with the unscented Kalman filter giving somewhat better results than the extended Kalman filter.

1. INTRODUCTION

Among the existing crystal growth techniques where the solid material is created without contacting the surrounding walls, the Czochralski (Cz) method stands out when commercial production of monocrystalline silicon is concerned. The Cz process was discovered in the early 1900's by Jan Czochralski, while he was investigating the crystallization rate of metals. Even though this technique has been around for almost a century, it has only found wide practical application during the last decades because of the development of semiconductor engineering and the solar industries. The principle is based on melting the source material in a crucible, which is usually made of quartz. Then, a rotating seed crystal mounted on a rod is dipped into the melt. As the seed comes in contact with the melt, the melt solidifies on the seed and takes on the same crystallographic orientation as the seed. The seed is then slowly withdrawn from the melt, and surface tension causes the formation of a meniscus which connects the crystal to the melt. As the crystal is withdrawn, the melt solidifies along the top of the meniscus, causing the crystal to grow. The surface along which the material solidifies is referred to as the (crystal-melt) *interface*. By precisely controlling the temperature gradients, rate of pulling and speed of rotation, it is possible to extract a large, single-crystal, cylindrical *ingot* from the melt. At the end, the ingot is sliced into very thin wafers, and each wafer is polished and cut into a specific shape, depending on the final application.

⋆ Supported by Prediktor AS, the Research Council of Norway and NorSun.

In [Rahmanpour et al., 2013], a simulation study using a physically motivated model for the Czochralski process was used to compare the performance of the Kalman Filter, the Extended Kalman filter and the Unscented Kalman filter. The conclusion on the achieved results in [Rahmanpour et al., 2013] showed that the latter two filters provide highly accurate state estimates with excellent noise suppression.

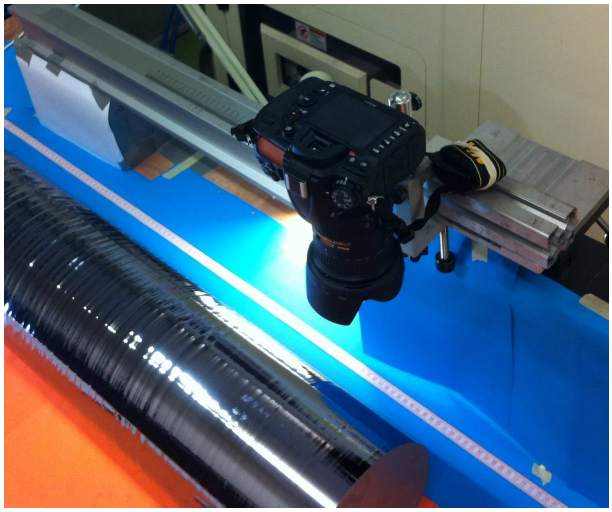

Fig. 1. The setup for taking photo of the edge of the ingot.

In continuation of the previous study, process data from a crystal puller has been collected. In addition to collecting on-line proceess data, the radius of the ingots were measured after production was finished. In order to do so, there was built a setup to correctly place the ingot and a

digital camera, as shown in Figure 1. With high quality pictures that was taken from the edge of the crystal and image processing techniques, the real changes in radius of the finished crystal resulted in an almost noise-free radius measurement.

With regard to [Rahmanpour et al., 2013], this paper further investigates and compares the performance of the Extended Kalman filter (EKF) and the Unscented Kalman filter (UKF), based on the collected process data, using the same physically motivated model for the Czochralski process. In addition, an attempt was made to tune the nonlinear filters based on the radius measurement from the ingot, while the real-time radius measurement was fed to the estimators.

The Cz process is briefly introduced with a simplified process model in section 2, while section 3 introduces EKF and UKF approaches and presents the implemented estimations methods used in this paper. The results of the applied estimators to the process model are presented at section 4, with further discussion and conclusion at section 5. Section 1 and subsection 2.1 in this paper are based on [Rahmanpour and Hovd, 2012] and subsection 2.2 is based on [Rahmanpour et al., 2013].

2. THE CZOCHRALSKI CRYSTALLIZATION PROCESS AND A MODEL FOR THE CRYSTAL RADIUS

2.1 Czochralski Process Description

A sketch of the Czochralski process is shown in Figure 2. Normally, a process run (i.e., production of a crystal) is initiated by placing an amount of solid silicon inside the crucible. As shown in Figure 2, the crucible is surrounded by the electrical heater used to melt the solid material and maintain an appropriate temperature trajectory during the crystallization.

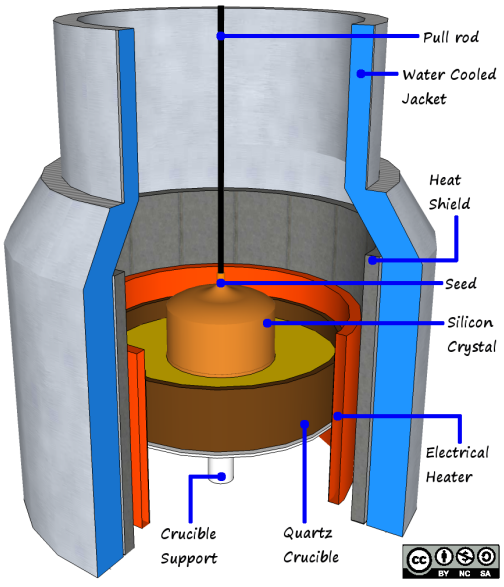

Fig. 2. An illustration of the main parts of the Czochralski crystallization process (This Figure is licensed under a Creative-Commons BY-NC-SA license).

The main part of the process starts when a small rotating crystal seed is lowered while it is hanging from the pulling wire and dipped into the molten silicon. The crystallization process takes place as the seed is slowly pulled out of the melt, while the pulling wire is counter-rotating with regard to the rotating crucible. Even though the crystal diameter is quickly increased at the beginning, it is desirable to keep the diameter constant for most of the process progression. A sketch of the region around the meniscus is shown in Figure 3.

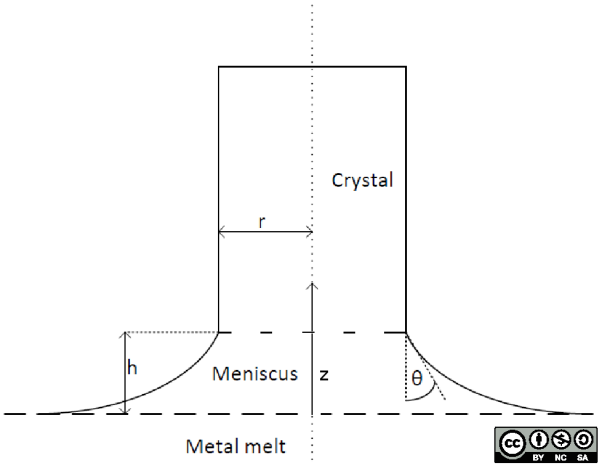

Fig. 3. A sketch of the crystal and its contact with the molten metal(This Figure is licensed under a Creative-Commons BY-NC-SA license).

2.2 A Crystal Formation Model for the Czochralski Process

The basic phenomena that need to be covered by a model for the Czochralski process are the *capillary problem* and the *thermal conditions*. From the theory of hydrostatics, the equilibrium shape of the liquid surface is described by the Laplace capillary equation [Tatarchenko, 1993]:

$$\frac{\sigma_{LV}}{R_1} + \frac{\sigma_{LV}}{R_2} + g\rho_L \tilde{z} = \text{const.} \tag{1}$$

where σ_{LV} is the liquid surface tension coefficient at the three-phase boundary, ρ_L denotes the liquid density, and R_1 and R_2 are the principal radii of curvature of the meniscus. The value of the constant is defined based on the selection of the origin of the $\tilde{z}$-coordinate and the difference between the pressure of the liquid p and gas p_v at the origin. Using the capillary constant $a = (2\sigma_{LV}/g\rho_L)^{1/2}$, we get a dimensionless coordinate $\tilde{z}/a = z$ where the $\tilde{z}$-axis is directed vertically upwards. The liquid surface meniscus for cylindrical or tubular crystals is obtained by rotating the profile curve around this axis. The shape of the free liquid surface is given by solution of the Laplace-Young equation [Tatarchenko, 1993]:

$$\begin{aligned} z^{''} r + z^{'}(1 + z^{'2}) \pm 2(d - z)(1 + z^{'2})^{3/2} = 0, \\ d = \frac{p \cdot a}{2\sigma_{LV}} \end{aligned} \tag{2}$$

In (2), r represents the radial coordinate, z defines the vertical coordinate and the Laplace constant is denoted by a.

A heat transfer balance about the interface states that the heat flow caused by crystallization (Φ_h) is given by the difference between the heat flow from the interface to the crystal (Φ_s) and the heat flow from the melt to the interface (Φ_l) [Winkler et al., 2010, pp. 1007,1012]:

$$\Phi_\mathrm{h} = \Phi_\mathrm{s} - \Phi_\mathrm{l} \tag{3}$$

where

$$\Phi_\mathrm{h} = \rho_\mathrm{s} v_\mathrm{g} A_\mathrm{i} \Delta H \tag{4a}$$
$$\Phi_\mathrm{s} = k_\mathrm{s} A_\mathrm{i} \nabla T_\mathrm{s} \tag{4b}$$
$$\Phi_\mathrm{l} = k_\mathrm{l} A_\mathrm{i} \nabla T_\mathrm{l} \tag{4c}$$

The latent heat of fusion is represented by ΔH, T_s and T_l denote the temperatures in the solid and the melt, respectively, the growth rate which is normal to the interface is denoted by v_g, ρ_s is the solid state density, k_s and k_l are the thermal conductivity coefficients in crystal and the melt, and A_i is the interface or meniscus area. Higher accuracy of the Cz model will require higher model complexity, involving coupled PDE's [Tatarchenko, 1993]. There exist such highly complicated and accurate simulation models with the quasi-stationary conditions as the fundamental design assumption. Such models are poorly suited for controller design, due to both the high complexity and the quasi-stationarity assumption.

Steel and Hill [1975, p. 49] and Hurle et al. [1990, p. 15] suggest the following estimate of the melt temperature gradient under the assumption that the heat radiation from the meniscus to the environment is negligible

$$\nabla T_\mathrm{l} \approx \frac{T_\mathrm{B} - T_\mathrm{M}}{h} \tag{5}$$

This results in the following expression for the melt-meniscus heat flow

$$\Phi_\mathrm{l} \approx k_\mathrm{l} A_\mathrm{i} \frac{T_\mathrm{B} - T_\mathrm{M}}{h} \tag{6}$$

Here T_B is the temperature at the base of the meniscus, T_M is the melting temperature (at the lower surface of the cylindrical crystal). Since, over time, the growth rate (v_g) equals the average pulling rate (v_p), the following estimate of the rate of heat release can be obtained from (4a) by assuming a flat interface:

$$\Phi_\mathrm{h} \approx \pi r_\mathrm{c}^2 \rho_\mathrm{s} \Delta H v_\mathrm{p} \tag{7}$$

In describing the dynamics of the crystal radius, the growth rate is the most important quantity. It can be calculated from the heat flow caused by crystallization (4a) as follows

$$v_\mathrm{g} = \frac{\Phi_\mathrm{h}}{\pi r_\mathrm{c}^2 \rho_\mathrm{s} \Delta H} \tag{8a}$$

where a flat interface has been assumed. By considering (3), (4b), (6) and (8a), the following expression for the growth rate is obtained

$$v_\mathrm{g} = \frac{1}{\rho_\mathrm{s} \Delta H} \left(k_\mathrm{s} \Delta T_\mathrm{s} - \frac{k_\mathrm{l}}{h} (T_\mathrm{B} - T_\mathrm{M}) \right) \tag{9}$$

where ΔT_s represents the temperature gradient in the crystal.

During growth, the radius (diameter) of the crystal is typically measured by a CCD camera aimed at the meniscus, which can be identified as a 'glowing ring' due to reflections from the glowing hot environment. However, the radius thus measured is sensitive to changes in meniscus height as well as waves on the melt surface. Since the CCD camera is calibrated to be aimed at the meniscus, the melt level must be the same at all time. Otherwise, the camera will not be able to detect the glowing ring. In practice, the melt level is not measurable, instead an approximate algorithm is used to find a lift ratio for the crucible, which should compensate for the changes in the melt level.

In this paper, an ideal assumption is taken into account where the vertical position of the melt level is kept constant, which means that the crucible lift rate is such that it compensates for the drop in melt level perfectly, leaving the following simple model [Hurle et al., 1989]:

$$\dot{\mathbf{x}} = \mathbf{f}(\mathbf{x}, \mathbf{u}) \tag{10a}$$
$$y = g(\mathbf{x}) \tag{10b}$$

with

$$\mathbf{f}(\mathbf{x}, u) = [f_1, f_2]^\top = [v_\mathrm{g} \tan\theta, v_\mathrm{p} - v_\mathrm{g}]^\top \tag{11a}$$
$$g(\mathbf{x}) = r_\mathrm{CCD}, \quad \mathbf{x} = [r_\mathrm{c}, h]^\top, \quad u = v_\mathrm{p} \tag{11b}$$

where θ defines the growth angle. For most of the crystal, the growth angle θ is small and nearly constant, but it cannot be measured during operation. Instead we replace it with the approximation [Duffar, 2010].

$$\sin(\theta) \approx 1 - \left(\frac{h}{a}\right)^2 \left(1 + \frac{a}{r\sqrt{2}}\right) \approx \theta \tag{12}$$

Here a, as above, represents the Laplace constant. In normal operation, the angle θ will stay within a few degrees from zero. Thus, we can use the approximation $\tan(\theta) \approx \sin(\theta) \approx \theta$ for $\theta \approx 0$.

A basic summary of the introduced equations can be the following: Meniscus geometry will strongly affect the heat transfer from the molten metal to the interface. Furthermore, the crystal growth angle and the crystal diameter will also be influence directly by the meniscus geometry. Consequently, the crystal diameter will influence the heat transfer from the interface to the environment. Thus, it is vital to control the proper shape of the melt meniscus, in order to pull an adequate crystal [Duffar, 2010].

Automated Cz growth requires multiple control loops, including loops for pressure, seed and crucible rotation rates and crucible lift rate control. However in the conventional control scheme, there are three control loops whose performance are strongly correlated with the crystal quality. The first one is a diameter controller which affects the diameter by manipulating the pulling rate, and uses feedback from diameter measurement to follow a desired target trajectory. The purpose of the second one is to ensure that the temperature conditions in the melt are satisfactory by manipulating the electrical heater which should follow an empirically predetermined setpoint trajectory. The third is the growth rate controller which is placed in cascade connection with the temperature controller, and adds offset to the temperature setpoint trajectory when the output (pulling rate) from the diameter controller differs from a pre-calculated pulling rate trajectory. These three controllers are usually PID controllers. To deal with the time-varying operating conditions, such as the decreasing melt

level, the parameters of the controllers change with time through gain scheduling.

Preferably, the estimators should estimate both states (r_c, h). Since the radius (r_c) is the only quantity that is measured (r_{CCD}), this will be the only measurement available for state estimation, and will have to allow updating of both crystal radius and meniscus height estimates. It will be found below that the model is indeed observable with this single measurement.

Linearized system dynamics The EKF requires a linearized model. Through Taylor series expansion of these equations, a standard LTI model is obtained

$$\dot{\bar{\mathbf{x}}} = \mathbf{A}\bar{\mathbf{x}} + \mathbf{B}\bar{u} + \mathbf{E}\bar{\mathbf{w}} \tag{13a}$$
$$\bar{y} = \mathbf{C}\bar{\mathbf{x}} + D\bar{u} + H\bar{v} \tag{13b}$$

with

$$\bar{\mathbf{w}} = \mathbf{w} - \mathbf{w}_0 = \mathbf{w} = [w_1, w_2]^\top = [0, v_{g,noise}]^\top \tag{14a}$$
$$\bar{v} = v - v_0 = v \tag{14b}$$

where

$$\mathbf{A} = \left.\begin{bmatrix} \frac{\partial f_1}{\partial r_c} & \frac{\partial f_1}{\partial h} \\ \frac{\partial f_2}{\partial r_c} & \frac{\partial f_2}{\partial h} \end{bmatrix}\right|_* = \begin{bmatrix} v_{g,0} \left.\frac{\partial \theta}{\partial r_c}\right|_* & v_{g,0} \left.\frac{\partial \theta}{\partial h}\right|_* \\ 0 & 0 \end{bmatrix}$$
$$\approx \begin{bmatrix} 0 & -2\frac{h_0}{a} v_{g,0} \\ 0 & 0 \end{bmatrix} \tag{15a}$$

$$\mathbf{B} = \left.\left[\frac{\partial f_1}{\partial u}, \frac{\partial f_2}{\partial u}\right]^\top\right|_* = [0, 1]^\top \tag{15b}$$

$$\mathbf{C} = \left.\begin{bmatrix} \frac{\partial g}{\partial r_c} & \frac{\partial g}{\partial h} \end{bmatrix}\right|_* = \left.\begin{bmatrix} \frac{\partial r_{CCD}}{\partial r_c} & \frac{\partial r_{CCD}}{\partial h} \end{bmatrix}\right|_*$$
$$\approx \begin{bmatrix} 1, \left.\frac{\partial r_{CCD}}{\partial h}\right|_* \end{bmatrix} \tag{15c}$$

$$\mathbf{D} = \left.\frac{\partial g}{\partial u}\right|_* = 0 \tag{15d}$$

$$\mathbf{E} = \left.\left[\frac{\partial f_1}{\partial w_1}, \frac{\partial f_2}{\partial w_2}\right]^\top\right|_* = \begin{bmatrix} 0 \\ -1 \end{bmatrix} \tag{15e}$$

$$\mathbf{H} = \left.\frac{\partial g}{\partial v}\right|_* = 1 \tag{15f}$$

and where $*$ indicates the points at which the expressions are evaluated, i.e., the linearization points. With these matrices, the observability and controllability matrices are respectively given by

$$\mathcal{O} \approx \begin{bmatrix} 1 & \left.\frac{\partial r_{CCD}}{\partial h}\right|_* \\ 0 & -2\frac{h_0}{a} v_{g,0} \end{bmatrix}, \quad \mathcal{C} \approx \begin{bmatrix} 0 & -2\frac{h_0}{a} v_{g,0} \\ 1 & 0 \end{bmatrix} \tag{16}$$

Both matrices have full rank for a positive growth rate. The system is therefore structurally always observable, since $\partial r_{CCD}/\partial h$ is always positive. This has been shown numerically in [Bones and Haugen, 2012].

3. STATE ESTIMATION

The meniscus height is not measurable and the measured radius is quite noisy. Thus, the actual radius and the meniscus height are not available during crystal growth. Therefore, use of feedback from estimators that attempt to compute these quantities are explored. Two types of state estimators are investigated: the extended Kalman filter and the unscented Kalman filter. It is common to convert the continuous-time model (f, g) to a discrete-time model (F, G) in order to implement the model in a computer. Therefore, the estimator equations in this section are illustrated in their discrete-time version. The following notation is used in this section:

- $\bar{\mathbf{x}}$ is the mean value of $\mathbf{x}$
- $\hat{\mathbf{x}}$ is the state estimate
- $\hat{\mathbf{x}}^-$ is the predicted (a priori) state estimate
- $\hat{\mathbf{y}}$ is the measurement estimate
- $\mathbf{P}$ is the estimate covariance
- $\mathbf{Q}$ is the covariance of the process noise
- $\mathbf{R}$ is the covariance of the observation noise
- $\mathbf{K}_k$ is the Kalman gain

3.1 Extended Kalman Filter Design

The *Extended Kalman Filter* (*EKF*) uses a nonlinear model to predict a new state estimate, and a local linearization of the nonlinear model is used to improve the state estimate when new measurements are available. In this case, the algorithm takes the following form [Brown and Hwang, 1997, pp. 343-347]

- **Step 1: Predict**

  Predict new state estimate
  $$\hat{\mathbf{x}}^-_{k+1} = \mathbf{F}(\hat{\mathbf{x}}_k, \mathbf{u}_k)$$
  Compute the error covariance of the new estimate
  $$\mathbf{P}^-_{k+1} = \mathbf{A}_{d,k}\mathbf{P}_k\mathbf{A}^\top_{d,k} + \mathbf{E}_{d,k}\mathbf{Q}_k\mathbf{E}^\top_{d,k}$$
- **Step 2: Update**

  Compute the Kalman gain
  $$\mathbf{K}_k = \mathbf{P}^-_k\mathbf{C}^\top_{d,k}\left(\mathbf{C}_{d,k}\mathbf{P}^-_k\mathbf{C}^\top_d + \mathbf{R}_{d,k}\right)^{-1}$$
  Update the state estimates
  $$\hat{\mathbf{x}}_k = \hat{\mathbf{x}}^-_k + \mathbf{K}_k\left[\mathbf{y}_k - \mathbf{G}\left(\hat{\mathbf{x}}^-_k, \mathbf{u}_k, k\right)\right]$$
  Compute the error covariance for the updated estimate
  $$\mathbf{P}_k = \mathrm{E}\left[\mathbf{e}_k\mathbf{e}^\top_k\right]$$
  $$= \left(\mathbf{I} - \mathbf{K}_k\mathbf{C}_{d,k}\right)\mathbf{P}^-_k\left(\mathbf{I} - \mathbf{K}_k\mathbf{C}_d\right)^\top + \mathbf{K}_k\mathbf{R}_{d,k}\mathbf{K}^\top_k$$

where the Jacobian matrices $\mathbf{A}_{d,k}$ and $\mathbf{C}_{d,k}$ are recalculated along the systems trajectories according to the discretization of

$$\mathbf{A}_{d,k} = \left.\frac{\partial \mathbf{F}}{\partial \mathbf{x}}\right|_{\hat{\mathbf{x}}_k, \mathbf{u}_k} \quad \text{and} \quad \mathbf{C}_{d,k+1} = \left.\frac{\partial G}{\partial \mathbf{x}}\right|_{\hat{\mathbf{x}}^-_{k+1}, \mathbf{u}_k}$$

3.2 Unscented Kalman Filter Design

In *Unscented Kalman Filter* (*UKF*), the state distribution is represented by a Gaussian random variable (GRV) which is specified using a minimal set of carefully chosen sample points (*sigma points*). These sample points completely

capture the true mean and covariance of the GRV, and when propagated through the true nonlinear system dynamics, capture the posterior mean and covariance accurately to the second order (Taylor series expansion) for any nonlinearity. The statistics of the transformed points can then be calculated to form an estimate of the nonlinearly transformed mean and covariance [Haykin, 2001].

It is noticeable that the sigma points are not chosen randomly; they are deterministically chosen so that they exhibit certain properties. Furthermore, the sigma points can be weighted [Julier and Uhlmann, 2004]. Assume propagating a random variable x of dimension L through $\mathbf{y} = \mathbf{f}(\mathbf{x})$ with mean and covariance defined above. To calculate the statistics of the propagated points ($\mathbf{y}$), a matrix χ of $2L+1$ sigma vectors χ_i is defined as [Haykin, 2001]:

$$\begin{aligned}\chi_0 &= \bar{\mathbf{x}},\\ \chi_i &= \bar{\mathbf{x}} + (\sqrt{(L+\lambda)\mathbf{P_x}})_i, \quad i = 1,\cdots,L\\ \chi_i &= \bar{\mathbf{x}} - (\sqrt{(L+\lambda)\mathbf{P_x}})_{i-L},\ i = L+1,\cdots,2L\end{aligned} \tag{18}$$

where $\lambda = \alpha^2(L+\kappa) - L$ is a scaling parameter. The constant α determines the spread of the sigma points around $\bar{\mathbf{x}}$, and is usually small ($1 \geq \alpha \geq 10^{-4}$). κ and β are also scaling parameters. $(\sqrt{(L+\lambda)\mathbf{P_x}})_i$ is the ith column of the lower-triangular Cholesky factorization. The UKF used in this paper is implemented as described in [Haykin, 2001], where a full description of this technique and how to select scaling parameters also can be found. The weights applied to the propagated sigma points and the UKF algorithm are defined as follows:

$$\begin{aligned}W_0^{(m)} &= \frac{\lambda}{L+\lambda},\\ W_0^{(c)} &= \frac{\lambda}{L+\lambda} + 1 - \alpha^2 + \beta,\\ W_i^{(m)} &= W_i^{(c)} = \frac{1}{2(L+\lambda)}, \quad i = 1,\cdots,2L\end{aligned} \tag{19}$$

- **Step 1: Initialize**

  Initialize with

  $$\begin{aligned}\hat{\mathbf{x}}_0 &= \mathbb{E}[\mathbf{x_0}],\\ \mathbf{P_0} &= \mathbb{E}[(\mathbf{x_0} - \hat{\mathbf{x}}_0)(\mathbf{x_0} - \hat{\mathbf{x}}_0)^\top].\end{aligned}$$

  For $k \in \{1,\cdots,\infty\}$, calculate the sigma points:

  $$\boldsymbol{\chi}_{k-1} = [\hat{\mathbf{x}}_{k-1} \quad \hat{\mathbf{x}}_{k-1} + \gamma\sqrt{\mathbf{P_{k-1}}} \quad \hat{\mathbf{x}}_{k-1} - \gamma\sqrt{\mathbf{P_{k-1}}}].$$

- **Step 2: Predict**

  The time-update equations are

  $$\begin{aligned}\boldsymbol{\chi}^*_{k|k-1} &= \mathbf{F}(\boldsymbol{\chi}_{\mathbf{k-1}}, \mathbf{u_{k-1}})\\ \hat{\mathbf{x}}_k^- &= \sum_{i=0}^{2L} W_i^{(m)} \chi^*_{i,k|k-1}\\ \mathbf{P}_k^- &= \\ &\sum_{i=0}^{2L} W_i^{(c)}(\chi^*_{i,k|k-1} - \hat{\mathbf{x}}_k^-)(\chi^*_{i,k|k-1} - \hat{\mathbf{x}}_k^-)^\top + \mathbf{Q}\end{aligned}$$

- **Step 3: Update**

  We redraw a complete new set of sigma points

  $$\begin{aligned}\boldsymbol{\chi}_{k|k-1} &= [\hat{\mathbf{x}}_k^- \quad \hat{\mathbf{x}}_k^- + \gamma\sqrt{\mathbf{P_k^-}} \quad \hat{\mathbf{x}}_k^- - \gamma\sqrt{\mathbf{P_k^-}}]\\ \boldsymbol{\mathcal{Y}}_{k|k-1} &= \mathbf{G}(\boldsymbol{\chi}_{\mathbf{k|k-1}})\\ \hat{\mathbf{y}}_\mathbf{k}^- &= \sum_{i=0}^{2L} W_i^{(m)} \mathcal{Y}_{i,k|k-1}\end{aligned}$$

  and the measurements-update equations are

  $$\begin{aligned}\mathbf{P_{y_k y_k}} &= \\ &\sum_{i=0}^{2L} W_i^{(c)}(\mathcal{Y}_{i,k|k-1} - \hat{\mathbf{y}}_\mathbf{k}^-)(\mathcal{Y}_{\mathbf{i,k|k-1}} - \hat{\mathbf{y}}_\mathbf{k}^-)^\top + \mathbf{R}\\ \mathbf{P_{x_k y_k}} &= \\ &\sum_{i=0}^{2L} W_i^{(c)}(\chi_{i,k|k-1} - \hat{\mathbf{x}}_\mathbf{k}^-)(\mathcal{Y}_{\mathbf{i,k|k-1}} - \hat{\mathbf{y}}_\mathbf{k}^-)^\top\\ \mathbf{K}_k &= \mathbf{P_{x_k y_k}}\mathbf{P_{y_k y_k}^{-1}}\\ \hat{\mathbf{x}}_k &= \hat{\mathbf{x}}_k^- + \mathbf{K}_k(\mathbf{y_k} - \hat{\mathbf{y}}_\mathbf{k}^-)\\ \mathbf{P_k} &= \mathbf{P_k^-} - \mathbf{K_k}\mathbf{P_{y_k y_k}}\mathbf{K_k^\top}\end{aligned}$$

  where $\gamma = \sqrt{L+\lambda}$ and W_i are the weights as calculated in (19).

4. SIMULATION RESULTS

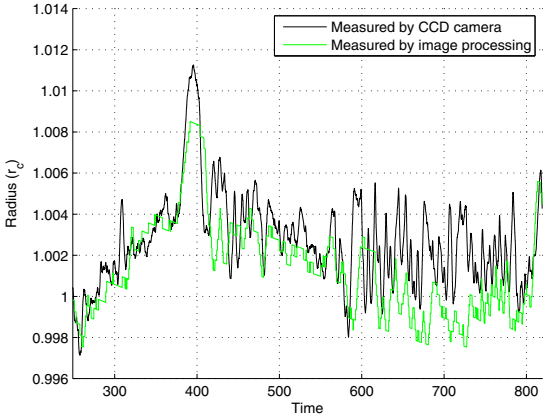

Fig. 4. Comparison of online measurment of crystal radius by CCD camera and the measured ingot radius using image processing tools.

Figure 4 shows the actual radius measured both during the pulling process and afterwards. When using a CCD camera for real-time radius measurement, it is quite noisy. In order to investigate how close the CCD camera measurement is to the true radius, it is interesting to measure the radius of the resulting ingot, when the crystallization process is over. Since the latter radius measurement is done without process disturbances, using photographs taken at a more appropriate angle, higher accuracy measurements of the ingot radius can be obtained.

Figure 5 and 6, both illustrate the ingot radius r_c estimated by the EKF and UKF. Based on Figure 5, both estimators have performed quite well. By inspecting Figure 6 and Table 1, it becomes more clear that the UKF has done a better job estimating r_c, compared to the EKF. Most probably, this better performance by the UKF is because of the more precise handling of the non-linearities within

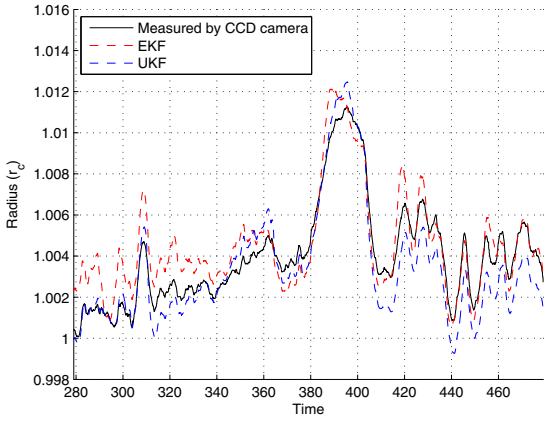

Fig. 5. Comparison of online measurment of crystal radius by CCD camera and the estimated radius using EKF and UKF.

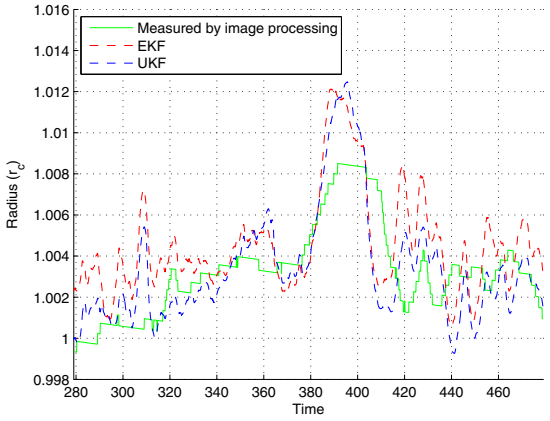

Fig. 6. Comparison of measured ingot radius and the estimated radius using EKF and UKF.

the model. In addition, this confirms that the existing non-linearities inside the model are capable of representing the actual process qualities.

The performance of these estimators was dependent on the accurate characterization of the uncertainties in the state dynamics and in the measurement. The parameters of the noise densities associated with these uncertainties were, however, treated as tuning parameters and were adjusted in an ad hoc manner while carrying out state estimation. It should be noted that both estimators used the same process noise and measurement noise covariance matrices and were tuned to fit the ingot radius while updating their estimates based on the CCD camera measurement. Equal importance were given to both estimators when selecting weight matrices, and it was found that similar noise densities gave good performance for both estimators.

Table 1. Root Mean Square Error of estimates

Observers	RMSE of $\hat{r}_c$
EKF	7.4042e-04
UKF	5.2499e-04

The overall performance of the estimators based on the deviation from the true ingot radius have been summarized in Table 1.

5. DISCUSSION AND CONCLUSIONS

The experimental results in this paper confirm the simulation based findings in [Rahmanpour et al., 2013]. It has been shown in this paper that the Kalman filters do an excellent job in dealing with measurement noise and provide acceptable estimates of both states. Advanced model-based control will require the model to be updated from measurements available on-line. The study confirms that both the EKF and UKF are capable of doing this. The differences between these two estimators are moderate, and practical issues may therefore dictate the choice of estimator. However, as the computational cost of both estimators are modest and comparable, the UKF would appear to be the preferred candidate. The good results of the two estimators, and the finding that the UKF (which does not linearize the model) performs better than the EKF, can be seen as an indication that the model captures the main non-linear effects in the plant well.

Plans for future work include applying the estimates in a model predictive control scheme.

REFERENCES

J.A. Bones and K. Haugen. Model-based control of the Czochralski Process. Master's thesis, Norwegian University of Science and Technology, 2012.

R.G. Brown and P.Y.C. Hwang. *Introduction to Random Signals and Applied Kalman Filtering.* John Wiley & Sons, third edition, 1997.

T. Duffar. *Crystal Growth Processes Based on Capillarity: Czochralski, floating zone, shaping and techniques.* John Wiley & Sons, 2010.

S. Haykin. *Kalman Filtering and Neural Networks.* John Wiley & Sons, 2001.

D.J. Hurle, G.C. Joyce, M. Ghassempoory, A.B. Crowley, and E.J. Stern. The dynamics of Czochralski Growth. *Journal of Crystal Growth*, 100:11–25, 1989.

D.J. Hurle, G.C. Joyce, M. Ghassempoory, A.B. Crowley, and E.J. Stern. The dynamics of Czochralski growth. *Journal of Crystal Growth*, 100(1-2):11–25, 1990. ISSN 0022-0248. doi: 10.1016/0022-0248(90)90603-I.

S. Julier and J. Uhlmann. Unscented filtering and nonlinear estimation. *Proceedings of the IEEE*, 92(3), 2004.

P. Rahmanpour and M. Hovd. Numerical backstepping for diameter control of silicon ingots in the Czochralski Process. 2012. Accepted to 51st IEEE Conference on Decision and Control, Maui, Hawaii.

P. Rahmanpour, J. A. Bones, M. Hovd, and J. T. Gravdahl. Linear and nonlinear state estimation in the Czochralski Process. 2013. Accepted to 10th IFAC Symposium on Dynamics and Control of Process Systems, Mumbai, India.

G.K. Steel and M.J. Hill. Analysis of the transfer function governing crystal growth in the Czochralski Process. *Journal of Crystal Growth*, 30(1):45 – 53, 1975. ISSN 0022-0248. doi: 10.1016/0022-0248(75)90198-0.

Y.A. Tatarchenko. *Shaped Crystal Growth.* Kluwer Academic Publishers, 1993.

J. Winkler, M. Neubert, and J. Rudolph. Nonlinear model-based control of the Czochralski process I: Motivation, modeling and feedback controller design. *Journal of Crystal Growth*, 312(7):1005–1018, 2010. ISSN 0022-0248. doi: 10.1016/j.jcrysgro.2009.12.074.